



New Anisotropic Cosmic-Ray Enhancement (ACRE) Event on 5 November 2023 Due to Complex Heliospheric Conditions

Agnieszka Gil¹ · Eleanna Asvestari² · Alexandar Mishev³ · Nicholas Larsen³ · Ilya Usoskin⁴

Received: 3 April 2024 / Accepted: 20 June 2024
© The Author(s) 2024

Abstract

The variability of galactic cosmic rays near Earth is nearly isotropic and driven by large-scale heliospheric modulation but rarely can very local anisotropic events be observed in low-energy cosmic rays. These anisotropic cosmic-ray enhancement (ACRE) events are related to interplanetary transients. Until now, two such events have been known. Here, we report the discovery of the third ACRE event observed as an increase of up to 6.4% in count rates of high- and midlatitude neutron monitors between ca. 09–14 UT on 5 November 2023 followed by a moderate Forbush decrease and a strong geomagnetic storm. This is the first known observation of ACRE in the midrigidity range of up to 8 GV. The anisotropy axis of ACRE was in the nearly anti-Sun direction. Modeling of the geomagnetic conditions implies that the observed increase was not caused by a storm-induced weakening of the geomagnetic shielding. As suggested by a detailed analysis and qualitative modeling using the EUHFORIA model, the ACRE event was likely produced by the scattering of cosmic rays on an intense interplanetary flux rope propagating north of the Earth and causing a glancing encounter. The forthcoming Forbush decrease was caused by an interplanetary coronal mass ejection that hit Earth centrally. A comprehensive analysis of the ACRE and complex heliospheric conditions is presented. However, a full quantitative modeling of such a complex event is not possible even with the most advanced models and calls for further developments.

Keywords Cosmic rays · Galactic · Coronal mass ejections · Interplanetary · Corona · Structures

1. Introduction

Galactic cosmic rays (GCRs) are highly energetic nucleonic particles omnipresent near Earth. Although their flux is considered isotropic and constant over time in the local interstellar matter, GCRs depict a great deal of variability in the vicinity of Earth on different

✉ I. Usoskin

¹ University of Siedlce, Siedlce, Poland

² Department of Physics, University of Helsinki, Helsinki, Finland

³ Sodankylä Geophysical Observatory, University of Oulu, Oulu, Finland

⁴ Space Physics and Astronomy Research Unit, University of Oulu, Oulu, Finland

timescales (e.g., Vainio et al. 2009) due to the heliospheric modulation caused by large-scale processes such as diffusion, convection, drifts, and adiabatic energy losses (e.g., Potgieter 2013).

On top of the relatively slow modulation, there are also sporadic fast variations of GCRs on the timescale of hours – days, caused by local transients. This includes Forbush decreases (FDs) caused by the passage of an interplanetary shock or magnetic flux rope near Earth (e.g., Cane 2000; Dumbović et al. 2022). A Forbush decrease is usually observed as a fast (within a few hours) significant (up to 25%), often two-step, drop in the count rate of a neutron monitor (NM) followed by a gradual recovery occurring over several days. The recovery phase is often anisotropic and exhibits pronounced diurnal variability in CRs due to the Earth's rotation. During Forbush decreases, the flux of GCRs up to high energy of tens of GeV can be affected (Jämsén et al. 2007; Usoskin et al. 2008). Moreover, a small enhancement of CR flux, called the FD preincrease, is sometimes observed prior to the FD onset as caused by the 'piling' of lower-energy CRs downstream of the approaching interplanetary shock (e.g., Belov et al. 2017; Papailiou et al. 2021). The preincrease is typically anisotropic with the maximum flux from the Sun's direction. Another type of fast sporadic cosmic-ray event is related to the transient flux of solar energetic particles (SEPs) produced by solar eruptions (e.g., Desai and Giacalone 2016; Reames 2017). SEP events with sufficiently energetic particles and high enough flux to be detected by NMs at ground level are called ground-level enhancements (GLEs: Poluianov et al. 2017). GLE events usually take several hours and can reach 5000% above the GCR background (the strongest known GLE took place on 23 February 1956 – see Usoskin et al. 2020b, and references therein).

Recently, a new type of transient cosmic-ray-variability event was discovered, the so-called anisotropic cosmic-ray enhancement (ACRE) event (Gil et al. 2018; Abunin et al. 2020). ACRE events are short (several hours) and small (a few per cent) highly anisotropic increases of GCRs in the vicinity of Earth as observed by high-latitude (low cutoff rigidity) NMs. Their anisotropy axes are not pointed to the Sun. Until recently, only two ACRE events were known – on 7 June 2015 and 26 August 2018 (see data at gle.oulu.fi). They are associated with enhanced scattering of low-energy cosmic rays on interplanetary magnetic structures (magnetized ejecta or magnetic rope) passing in the vicinity of Earth without directly hitting it (Gil et al. 2018).

Here, we report the third ACRE event that took place on 5 November 2023 and present a comprehensive analysis of the geomagnetic and heliospheric conditions during the event. In Section 2, data from the world network of NMs are presented and analyzed. Magnetospheric and near-Earth heliospheric conditions during the event are discussed in Sections 3 and 4, respectively. Discussion and conclusions are given in Section 5.

2. Neutron-Monitor Data

We employed records from a specifically designed network of ground-based detectors, that is the worldwide NM network. The NM was introduced during the International Geophysical Year (IGY) 1957 – 1958 as the basic detector for registration of cosmic-ray (CR) variations (Simpson 1957), however, several NM stations were operational even before 1956 (Simpson, Fonger, and Treiman 1953). In the mid-1960s, the design of the IGY NM was greatly improved by the introduction of NM-64, or supermonitor (Hatton and Carimichael 1964; Carmichael et al. 1968), nowadays the standard detector in the global NM network (e.g., Simpson 2000, and references therein). Currently, the records of most of the NMs are available in nearly real time from the NM database NMDB (nmdb.eu – see, e.g., Mavromichalaki

et al. 2011). The count rate of an NM located at a given altitude h and time t is defined as a superposition of its integral responses to different GCR species (Clem and Dorman 2000):

$$N(P_c, h, t) = \sum_i \int_{P_c}^{\infty} S_i(P, h) J_i(P, t) dP, \quad (1)$$

where P_c and h are the geomagnetic cutoff rigidity and the atmospheric depth (altitude above sea level), respectively, of the NM location, $S_i(P, h)$ [$\text{m}^2 \text{sr}$] is the NM yield function for primaries of particle type i (protons and/or α -particles), $J_i(P, t)$ [$\text{GV m}^2 \text{sr s}$] $^{-1}$ is the rigidity spectrum of the primary particle of type i at time t , where t accounts for the modulation effects, and the integration is over the particle's rigidity P . Sea-level NMs have the so-called atmospheric energy cutoff of about 1 GeV nuc^{-1} , which is significantly reduced to about 300 MeV/nuc for high-altitude NMs such as DOMC and SOPO (e.g., Mishev and Poluianov 2021, and the discussion therein).

We have analyzed count rates, corrected for the barometric pressure and efficiency, of all the available mid- and high-latitude NMs for the period between 4 and 6 November 2023 with a special focus on the day of 5 November 2023 (day-of-year, DOY 309). We have also checked with GOES data that there was no ($> 30 \text{ MeV}$) SEP event during DOY 309.

Polar NMs are characterized by narrow asymptotic cones. Therefore, polar NMs naturally have better angular resolution than the bulk of midlatitude NMs, leading to their higher sensitivity to small variations of CR flux (e.g., Bieber et al. 2004; Mishev and Usoskin 2020).

The list of the analyzed NMs with the geomagnetic cutoff rigidities ranging from no-cutoff to 9 GV is given in Table 1. The data were collected from the Neutron Monitor Database (NMDB: www.nmdb.eu/nest) and from individual NM websites as specified in the Acknowledgements. Count rates of all NMs were taken with 10-min resolution and normalized to the mean level for the day of 5 November 2023.

Since the event occurred on the background of large cosmic-ray fluctuations, including a Forbush decrease and diurnal variation, the data needs to be corrected for the variable background, viz. detrended, in a way similar to that used by Usoskin et al. (2020a). We evaluated the background as a second-order polynomial fitted for the count rates during the day of 5 November 2023 excluding the expected event time of 09–14 UT, which is denoted by the gray-shaded bar in Figure 1. Examples of the thus-defined background are shown in the figure as red curves. The background trend appears always decreasing because of the onset of the Forbush decrease, but the shape varies between different NMs. The verified dataset of original and detrended NM count rates for the ACRE event has been made publicly available at the International GLE Database (IGLED: gle oulu.fi). The intensity of the ACRE event was quantified as the event-integrated increase (the area between the detrended count rate and the baseline during the event – see Figure 1) expressed in the units of %h.

Each NM accepts CR particles from a narrow cone, called the acceptance cone (AC), on the celestial sphere as defined by the magnetospheric propagation of high-energy particles (e.g., Smart, Shea, and Flückiger 2000; Mishev, Poluianov, and Usoskin 2017). ACs of the NMs analyzed here are shown in Figure 2 for the time of the ACREs maximum (12 UT on 5 November 2023). The ACs were calculated using the OTSO (Open-source geomagneToSphere prOpagation tool) magnetospheric model (Larsen, Mishev, and Usoskin 2023). For the OTSO computations, the magnetosphere was modeled using a combination of the IGRF13 and Tsyganenko 01 (TSY01) models (Tsyganenko 2002; Alken et al. 2021), which is a typical combination used to represent a greatly disturbed geomagnetosphere, e.g., K_p index ≥ 5 . The TSY01 model is parameterized using solar-wind speed, dynamic pressure, interplanetary magnetic-field (IMF) strength in the y - and z -axis (B_y and B_z), Dst index,

Table 1 List (arranged via ascending order of the cutoff rigidity P_c) of neutron monitors used in this study. Columns represent the site's name; acronym; detector type; vertical cutoff rigidity (in GV); altitude (in meters a.s.l.); geographical latitude and longitude (in degrees); and intensity I of the ACRE (in %h), respectively. Acronyms and locations of the NMs are provided according to NMDB.

Name	Acronym	Type	P_c	Height	Lat	Lon	I
Dome C	DOMC	Mini-NM	0	3233	-75.1	123.3	0.9
Terre Adelie	TERA	9NM64	0	32	-66.7	140	0.4
Thule	THUL	9NM64	0	260	76.6	-68.4	1.7
Mirny	MRNY	12NM64	0	30	-66.55	93.02	1.0
South Pole	SOPO	3NM64	0.1	2820	-90	-	0.7
Mawson	MWSN	18NM64	0.22	30	-67.6	62.88	1.0
Nain	NAIN	18NM64	0.3	46	56.6	-61.7	1.1
Peawanuck	PWNK	18NM64	0.3	53	55	-85.4	1.0
Tixie Bay	TXBY	18NM64	0.3	0	71.6	128.9	0.5
Fort Smith	FSMT	18NM64	0.3	21	60.02	-111.93	2.0
Inuvik	INVK	18NM64	0.3	21	68.36	-133.72	0.5
JangBogo	JBGO	5NM64	0.3	29	-74.6	164.2	1.0
Apatity	APTY	18NM64	0.5	177	67.6	33.3	1.8
Oulu	OULU	9NM64	0.7	15	65.1	25.5	3.2
Yakutsk	YKTK	18NM64	0.85	105	62.01	129.43	1.2
Calgary	CALG	3NM64	0.9	1123	51.08	-114.13	0.6
Kerguelen	KERG	18NM64	1.1	0	-49.4	70.3	1.5
Moscow	MOSC	24NM64	1.74	200	55.47	37.32	4.0
Kiel	KIEL	18NM64	1.98	54	54.34	10.12	6.3
Novosibirsk	NVBK	24NM64	2.03	163	54.48	83	6.4
Newark	NEWK	9NM64	2.55	50	39.68	-75.75	2.2
Dourbes	DRBS	9NM64	3.09	225	50.1	4.6	4.7
Irkutsk3	IRK3	6NM64	3.16	3000	51.29	100.55	4.7
Lomnický Štit	LMKS	8SNM15	3.41	2634	49.2	20.22	3.7
JungfrauJoch	JUNG1	3NM64	4.44	3475	46.55	7.98	3.4
Baksan	BKSN	6NM64	5.6	1700	43.28	46.69	4.1
Alma-Ata B	AATB	18NM64	5.72	3340	43.13	76.55	1.4
Potchefstroom	PTFM	15IGY	6.9	1351	-26.7	27.1	2.3
Athens	ATHN	6NM64	8.14	260	37.97	23.78	2.3
Mexico City	MXCO	6NM64	8.2	2274	19.33	-99.2	1.2

G1 and G2 (G1 and G2 being parameters computed explicitly for the use of the TSY01 model requiring solar-wind data for the hour preceding the event (for details, see Tsyganenko 2002); with values of 438.4 km s⁻¹, 7.2 nPa, 5.9 nT, 25.8 nT, -90.0 nT, 0.16, and 0, respectively. Solar-wind data were taken from the Advanced Composition Explorer (ACE) satellite (sohofpt.nascom.nasa.gov/), with the 1-h averages used for the hour preceding the event to account for the time delay caused by solar wind traveling from the upstream L1 point, where ACE is located, to Earth. The Dst index for the time of the event was taken from the World Data Center for Geomagnetism (wdc.kugi.kyoto-u.ac.jp/). One can see that the ACs for most of the NMs lie in the tropical region ($\pm 30^\circ$ geographical latitude) covering the entire range of geographical longitudes. There are a few NMs that probe higher latitudes,

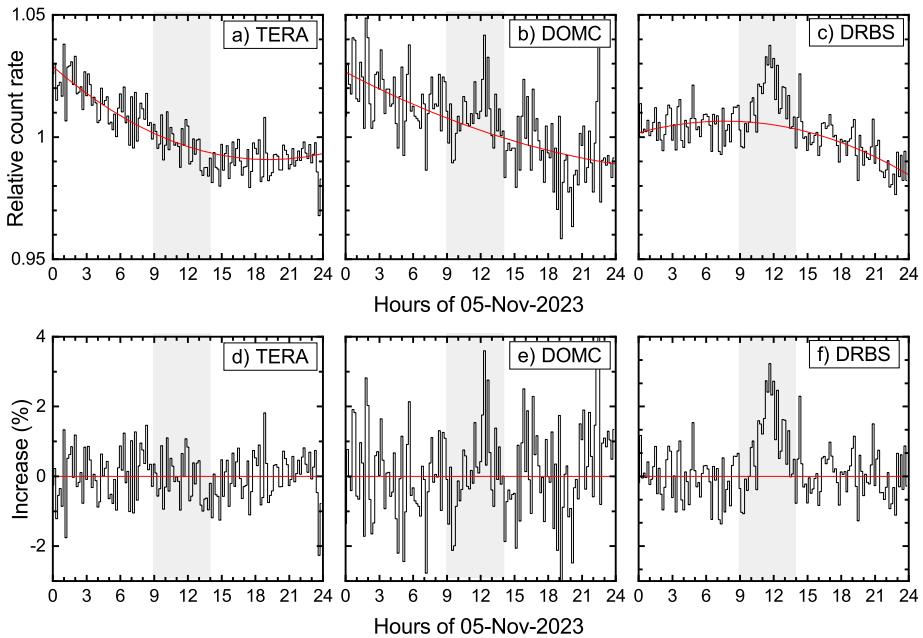


Figure 1 Normalized relative 10-min averaged pressure-corrected count rates of selected neutron monitors during DOY 309 (5 November) 2023. The upper row shows the raw data (black lines) with the fitted background trend (red curves – see text for details). Panels a–c represent typical cases of no event observed (TERA NM), a marginally defined event (DOMC) and a significantly defined event (DRBS). The lower row (panels d–f) depicts the detrended data corresponding to panels a–c. The gray-shaded bars denote the time of the event studied here, viz. 09–14 UT.

viz. DOMC (nearly polar acceptance cone), MRNY, TERA, JBGO, and SOPO in the Southern hemisphere, and only THUL in the Northern hemisphere. Interestingly, SOPO located at the geographical South Pole has the AC at midlatitudes because of the magnetospheric transport. With the worldwide network of NMs, we can probe the entire 3D picture of the CR flux (e.g., Bieber et al. 2004).

Due to the rotation of Earth whose axis is inclined with respect to the ecliptic plane, the geographical distribution of the ACs is not representative of CRs in the ecliptic plane. Figure 3 presents the measured ACRE signal projected onto the GSE (Geocentric Solar Ecliptic) coordinate system, where the location and size of symbols correspond to the NMs’ asymptotic directions at the geomagnetic cutoff rigidity P_c (2 GV for high-latitude NMs) and the intensity of the ACRE signal, respectively. Mid- and high-latitude NMs are denoted by blue and red circles, respectively. One can see that the ACRE response is distributed inhomogeneously over the celestial sphere, implying significant anisotropy of the effect. The maximum response is confined to the nearly anti-Sun direction (GSE longitude about 180°) in the ecliptic plane.

We have tested a simple fit to the data shown in Figure 3 by assuming a sum of the isotropic and anisotropic components, the latter is represented by a Gaussian distribution on the celestial sphere, so that the modeled ACRE signal S is approximated by

$$S = A_0 + A_1 \cdot \exp\left(\frac{-R^2}{2\sigma^2}\right), \tag{2}$$

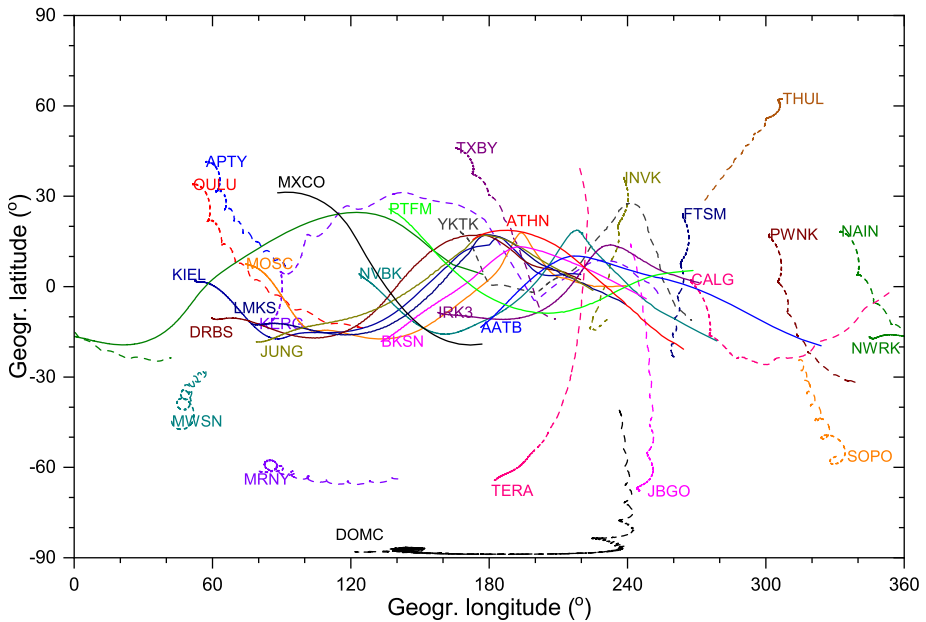


Figure 2 Asymptotic directions (in geographical coordinates) of the NMs considered here (see Table 1) computed using the OTSO code for 12 UT of 5 November 2023. Solid and dashed lines denote mid- and high-latitude NMs, respectively. Locations of the NM acronyms denote the high-rigidity (10 GV) end of the asymptotic direction, while the other end corresponds to the cutoff rigidity (1 GV for high-latitude NMs).

where A_0 is the isotropic component (in %h), A_1 is the magnitude of the anisotropic increase (in %h), R is the angular distance from the anisotropy axis, and σ is the width of the anisotropy angular distribution in GSE coordinates. The fit was done by minimizing the RMSE (root mean square error) discrepancy between the NM responses (intensity I) modeled by the function S and the measured ones. The best-fit parameters were found as $A_0 = 1 \pm 0.2\%h$; $A_1 = 3.3 \pm 0.2\%h$; $\sigma = 50^\circ \pm 4^\circ$; the location of the anisotropy axis has the latitude $-1.9^\circ \pm 1.1^\circ$ and longitude $157^\circ \pm 3^\circ$ in GSE coordinates. This is shown in Figure 3 as the magenta star and the 1σ contour.

Summarizing the analysis of NM data, we conclude that the ACRE was a highly anisotropic CR event with the anisotropy axis being close to the anti-Sun direction in the ecliptic plane.

3. Magnetospheric Conditions

Since the NMs are located on the ground and detect atmospheric nucleonic cascades induced by primary CRs after their transport in the magnetosphere, we need first to analyze the magnetospheric condition during the time of the event and check whether the detected increase could be caused by the magnetospheric effect due to a reduced geomagnetic shielding. The access of a CR through the magnetosphere depends on many factors, including the particle's rigidity, location, and direction of its incidence as well as geomagnetic conditions. The geomagnetic shielding is usually quantified by the geomagnetic cutoff rigidity P_c so that particles with rigidity above/below the cutoff can/cannot penetrate the atmosphere at a given

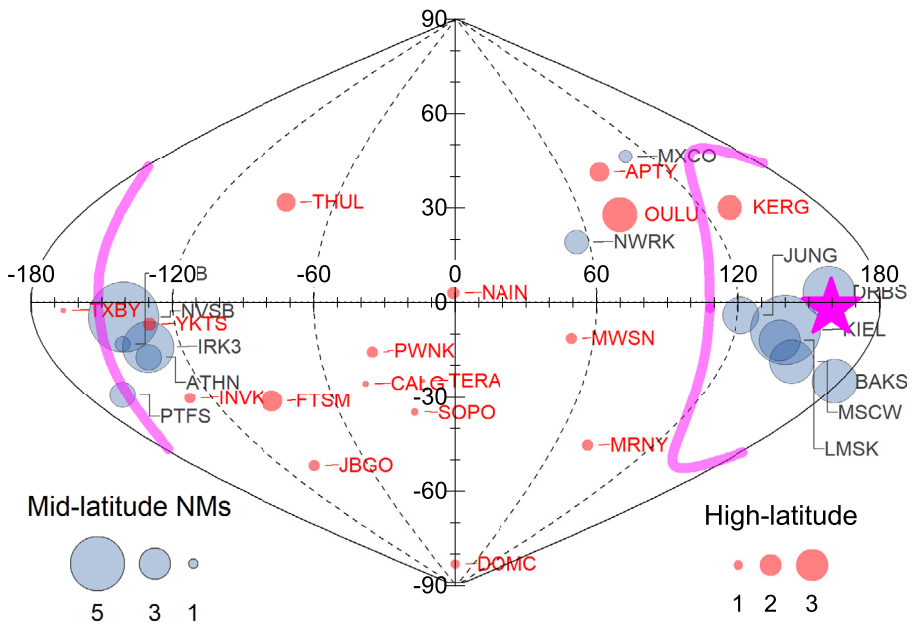


Figure 3 Map (sinusoidal projection, GSE coordinates) of the ACRE responses of the NMs at high ($P_c < 2$ GV, red circles) and midlatitudes (blue circles). The coordinates of the points correspond to the asymptotic directions of the NM at the rigidity $P^* = \max(2 \text{ GV}, P_c)$. The size of the symbols represents the intensity in %h (see Table 1) as indicated in the bottom panel. The magenta star and the thick curve depict the fitted (see Equation 2) anisotropy axis and its 1σ interval, respectively.

location (for details see, e.g., Cooke et al. 1991; Smart, Shea, and Flückiger 2000). During geomagnetic storms, the cutoff rigidity can be reduced, leading to a small increase of the incident CR intensity (e.g., Büttikofer 2018, and references therein). Even during the strongest geomagnetic storms, the P_c values can be reduced globally by at most 1 GV (Kudela, Bučík, and Bobík 2008). In such a case, the CR increase can be observed globally at low and mid-latitude NMs but not at high-latitude NMs where the geomagnetic shielding is anyway weak or absent.

The geomagnetic conditions during the events are shown in Figure 4a through the changes in the 10-min averaged SymH geomagnetic index that describes the geomagnetic disturbances at midlatitudes with high temporal resolution. It is a longitudinally symmetric disturbance index derived for the horizontal geomagnetic-field component H (Iyemori et al. 1996). The SymH index is similar to the hourly Dst-index (Sugiura and Poros 1971) but composed based on one-minute values from different collections of stations and a slightly different coordinate system. The SymH is calculated by averaging the disturbance component for each minute based on exactly six stations from the set: Alibag, Boulder, Chambon-la-Foret, Fredericksburg, Hermanus, Honolulu, Martin de Vivies, Memambetsu, San Juan, Tucson, and Urumqi (Iyemori et al. 1996). Indeed, the analyzed event occurred on the background of a moderate geomagnetic storm with the lowest SymH value being about -100 nT, however, even a stronger disturbance with a minimum value of -189 nT took place later at about 17 UT on 5 November 2023. To check this possibility, we have calculated the geomagnetic cutoff rigidity P_c as a function of time around the ACRE event for each NM, as exemplified in Figure 4b for the Durbes NM. As seen, the P_c value was slightly lower

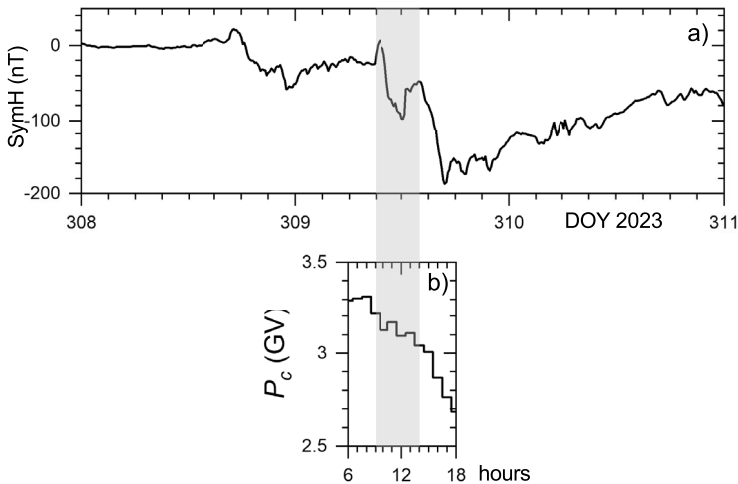


Figure 4 Geomagnetic conditions around the ACRE event. Panel a depicts the 10-min SymH geomagnetic data (omniweb.gsfc.nasa.gov/) for the period of 4–6 November (DOY 308–310) 2023. Data are shown as 10-min values for the period of 4–6 November (DOY 308–310) 2023. The time interval of the studied event (09–14 UT on 5 November 2023) is shaded. Panel b depicts the effective cutoff rigidity changes of the Dourbes NM around the studied event (indicated by the shaded area) as computed by the OTSO model.

during the event (by ≈ 0.2 GV) than before it, but its count-rate effect is too small ($< 1\%$). A stronger reduction of P_c by about 0.6 GV was observed later during the day as induced by the geomagnetic storm, but it was too late to be related to the ACRE event.

Thus, we conclude that the ACRE event of 5 November 2023 cannot be explained by a geomagnetic effect for the following reasons: (i) the time profile of the weakening of the geomagnetic shielding did not correspond to the ACRE time profile; (ii) ACRE was observed not only at midlatitude but also at polar stations where the geomagnetic shielding is negligible; (iii) the ACRE event was highly anisotropic with a narrow ($\approx 50^\circ$) cone, which is not expected for the geomagnetic effect.

4. State of the Heliosphere

Next, we considered the heliospheric conditions during and around the day of 5 November 2023.

The Sun was particularly active for several days preceding the event, viz. 31 October 2023 through 4 November 2023, with a number of Coronal Mass Ejections (CMEs) identifiable in white-light coronagraph images. CMEs can strongly disturb the interplanetary magnetic field and plasma conditions, potentially affecting the transport of GCRs near Earth. To understand this, we simulated the heliospheric conditions during the passage of the Interplanetary CME (ICME) structures using the magnetohydrodynamic (MHD) Space-Weather forecasting model EUHFORIA (EUropean Heliospheric FORecasting Information Asset – see Pomoell and Poedts 2018; Poedts et al. 2020). To initiate the EUHFORIA simulation we first identified the CME events that might be relevant for the near-Earth conditions at the ACRE time and subsequently deduced their geometric and kinematic parameters via 3D reconstructions of the CME in white-light images. Considering that STEREO-A and SOHO

were only approximately 5.6° apart during that period of time, thus observing the interplanetary structures from almost the same vantage point, we anticipate that the 3D reconstructions will only provide a rough estimate of their properties necessary to initiate EUHFORIA. For the same reason, we also limited our analysis to the use of the StereoCAT tool (ccmc.gsfc.nasa.gov/tools/StereoCat/) when reconstructing the geometry of the CMEs in the white-light observations. We note that for some of the eruptions, the white-light signatures were faint and/or narrow, and on two occasions, multiple eruptions made it difficult to fit the structures for multiple time steps and/or define their boundaries with good accuracy. This introduces additional uncertainties in the kinematic and geometric parameters defined by the 3D reconstructions with StereoCAT. Nevertheless, the analysis provides a reasonable set of input parameters for the CME models in EUHFORIA.

By analyzing white-light images from the Large Angle and Spectrometric CORonagraph (LASCO: Brueckner et al. 1995) C2 telescope on board the Solar and Heliospheric Observatory (SOHO: Domingo, Fleck, and Poland 1995), and by the SECCHI – COR2 coronagraph on board the A spacecraft of the Solar Terrestrial Relations Observatory (STEREO-A: Kaiser 2005; Kaiser et al. 2008), we identified 16 CMEs that could potentially be relevant for our analysis. For six of them, the source locations were at the limb – four at the East and two at the West limb. Seven CMEs originated from the solar disk in the field-of-view (FOV) of Earth and therefore might have impacted our planet. Lastly, for three CMEs no source was detected in the Earth's FOV and thus we consider them as back-sided events. One of these events was suspected, according to the performed 3D reconstruction analysis with StereoCAT, to have erupted on the disk behind the Earth's FOV and at high latitudes in the Southern hemisphere of the Sun. We, therefore, anticipate that part of the expanding structure could have potentially disturbed the southern heliosphere in the Earth's direction. Consequently, out of the three back-sided CME events we only considered the latter in our analysis. In Table 2 we list the kinematic and geometric parameters estimated from the 3D reconstructions with StereoCAT for all events.

To trace the parameters of the ambient solar wind and IMF with EUHFORIA, we used, as the inner boundary for the EUHFORIA coronal model, global photospheric magnetic-field maps from Air Force Data Assimilative Photospheric Flux Transport (ADAPT: Arge et al. 2010), provided by the Global Oscillation Network Group (GONG: gong.nso.edu/adapt/maps/gong/2023/). All CMEs were inserted in the heliospheric domain of EUHFORIA as a hydrodynamic pulse (cone model) apart from one of the on-disk eruptions in the FOV of Earth that was simulated as a spheromak (Verbeke, Pomoell, and Poedts 2019) to properly model its magnetic-field topology. This eruption had a low inclination and a wide longitudinal extent from the location of its source centered at approximately 22° in longitude and 30° in latitude in Stonyhurst coordinates and could be magnetically connected to Earth. For this reason, we opted to model that CME with the spheromak implementation in EUHFORIA. This gives us the ability to reconstruct also the magnetic flux rope embedded inside the magnetic cloud. Column 7 of Table 2 denotes the CME model considered in EUHFORIA for each studied eruption. For the cone CME models, the input plasma mass density and temperature were selected to be the default EUHFORIA values that are $1.1 \times 10^{-18} \text{ kg m}^{-3}$ and $0.8 \times 10^6 \text{ K}$, respectively. In the case of the event simulated as a spheromak, we need to define additional parameters to the geometric and kinetic ones. These parameters characterize the flux rope and are the magnetic flux, its chirality (also known as helicity sign), and its orientation angle. For the magnetic flux, we used the default value of $8 \times 10^{13} \text{ Wb}$, which is used in EUHFORIA when the flux-rope poloidal and toroidal magnetic fluxes are not easily or possible to be determined. Based on the X-ray and EUV signatures on the solar disc associated with the erupted flux rope, such as sigmoids and flare ribbons (Palmerio

Table 2 Geometric and kinematic parameters of the modeled CMEs, as extracted by 3D reconstructions of the white-light signatures with StereoCAT. The columns are: (1) the CME number used in this work; (2) time T_0 (in UTC) when the CME passed the distance of 2.5 solar radii; (3–5) longitude and latitude in Heliocentric Earth Equatorial (HEEQ) coordinates, and half-width (all in $^\circ$) of the CME; (6) speed (in km s^{-1}); and (7) the used EUHFORIA CME model.

CME #	Time T_0	Lon	Lat	Half-width	Speed	EUHFORIA
1	01-Nov 02:15	2	-37	29	874	cone
2	01-Nov 02:59	-82	-2	35	689	cone
3	01-Nov 06:49	-97	3	10	363	cone
4	01-Nov 20:35	-86	3	16	545	cone
5	02-Nov 08:52	-29	42	36	674	cone
6	02-Nov 16:48	-80	-18	23	471	cone
7	03-Nov 07:57	22	30	79	844	spheromak
8	03-Nov 09:42	50	6	20	345	cone
9	03-Nov 12:07	164	-48	56	387	cone
10	03-Nov 17:50	104	-38	41	504	cone
11	03-Nov 23:11	-9	-50	9	451	cone
12	04-Nov 01:18	90	-20	10	586	cone
13	04-Nov 14:43	42	48	13	234	cone
14	04-Nov 14:44	85	65	46	304	cone

et al. 2017), we determined that the erupted flux rope had a negative chirality. This is consistent with the hemispheric rule (Pevtsov and Balasubramaniam 2003; Wang 2013). The orientation of the spheromak upon insertion was determined based on the orientation of the polarity-inversion line (PIL) with respect to the solar equator, as identified based on EUV and magnetogram observations. Taking into account the spheromak insertion orientation as described by Asvestari et al. (2021, 2022), we determined the insertion orientation angle to be 45° . To prevent the spheromak from rotating due to the torque force exerted on it when it is inserted in the IMF (see Asvestari et al. 2022, for details on this phenomenon), we opted for a heavier spheromak, as recommended in Asvestari et al. (2022) and tested in Sarkar et al. (2024). For that purpose, the insertion spheromak mass density was selected as $0.5 \times 10^{-17} \text{ kg m}^{-3}$. The insertion temperature of the spheromak was selected to be the same as for the cone model.

Some plasma and magnetic-field conditions at the Earth's location are shown in Figure 5. A full set of in-situ data from the L1 point is shown in Figure 7 in the Appendix. The red curves indicate the data from OMNI database (King and Papitashvili 2005) while the blue curves are based on the EUHFORIA output. Both OMNI and EUHFORIA time series are shifted by 62 min to bring them closer to near-Earth conditions. In addition, the EUHFORIA time series has been shifted by 3.5 h so that the peak time in the EUHFORIA speed profile matches the peak time in the OMNI time series. This time difference in the modeled and in situ time series is well within the simulation accuracy for Space-Weather forecasting models (Riley et al. 2018; Verbeke et al. 2019). The peak in solar-wind speed corresponds to the spheromak (CME #7 in Table 2) whose southern flank passed Earth between 08:29 and 16:29 on 5 November. Despite this shift, the velocity rise began slightly earlier in the simulation than in the OMNI time series. This is due to the formation of a narrow sheath in the simulation domain. It is important that the model captured the magnetic-field rotation profiles well, and consequently the flux-rope rotation, even though the amplitude of the mod-

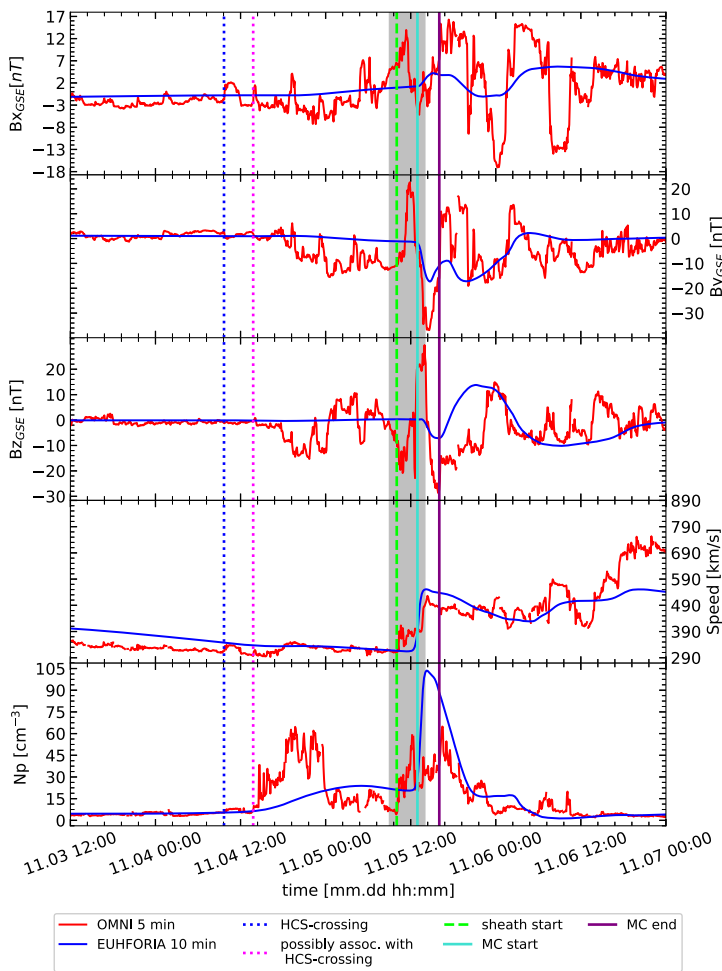


Figure 5 Plasma and magnetic-field conditions at Earth in 5-min OMNI data (red curve) and as simulated with EUHFORIA (blue curve). The blue curves in all panels are adjusted by 3.5 h to match the peak velocity for the event in both OMNI and EUHFORIA time series. The OMNI-based data were measured at the L1 point and translated to the near-Earth conditions by applying a 62-min delay corresponding to the propagation time from the L1 point for $V = 400 \text{ km s}^{-1}$. This shift is also applied to EUHFORIA output. The gray bar denotes the time interval of the ACRE (09–12 UT on 5 November 2023). The blue dotted line indicates a HCS crossing, and the magenta dotted line denotes signatures in the data that are indicative of a HCS crossing as well. The green dashed line indicates the start of the sheath region, while the start and end of the magnetic cloud (MC), also referred to as magnetic obstacle in the text, are indicated with cyan and purple solid lines, respectively.

eled magnetic components does not match the in situ measurements well. This mismatch in amplitude is most likely related to the input magnetic flux; however, given the good match in the profiles, we did not explore additional simulations, since the latter are computationally expensive. In both Figures 5 and Figure 7 we mark the sheath start in OMNI data with a green dashed line. This time was determined based on the increase in density, velocity, temperature, plasma beta, Mach number, and flow pressure. Accordingly, the drop in most of these parameters marks the start of the magnetic obstacle – MO (cyan solid line). The

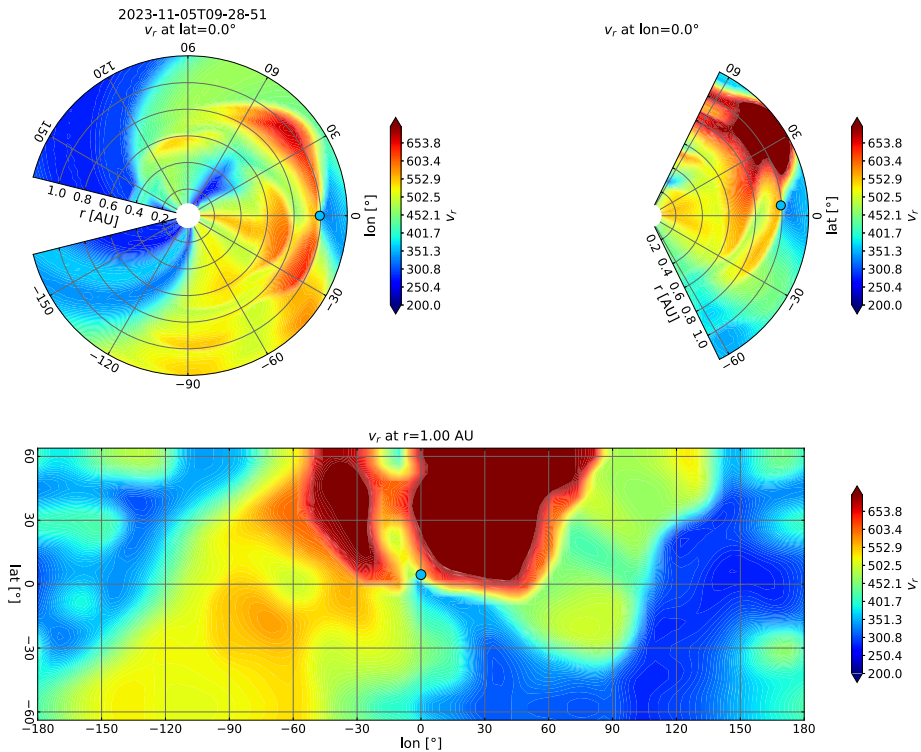


Figure 6 Near-Earth environment on 5 November at 09:28:51, simulated with EUHFORIA and represented in HEEQ coordinates (see Section 4) when the sheath formed in the simulation domain by CME 7 (spheromak – see Table 2) reached Earth from the solar North-West. CME #8 can be seen approaching in the solar North-East. The top-left/top-right images show the interplanetary solar-wind speed conditions in the ecliptic and Earth’s meridional planes, respectively. The bottom image depicts the solar-wind speed at the spherical shell at the radial distance of 1 AU from the Sun represented in 2D.

end of the MO is indicated by a solid purple line. It is important to mention that the signatures associated with this eruption are not those of a textbook event, and are presented with complicated characteristics. Thus, there is a degree of ambiguity when determining these boundaries. Our simulation output suggests that the other 13 CMEs from Table 2, modeled as hydrodynamic pulses, had the following features: CME #1 propagated southward from Earth and was only a glancing encounter on 4 November at 15:59; CME #8 was also Earth directed and impacted Earth at the same time as CME #7 (spheromak CME); CME #11 propagated through the heart of a high-speed stream and was also glancing at Earth on 6 November 16:28. CMEs #2–6, 9–10, and 12–14 did not have a direct impact on Earth, but they filled up the interplanetary space from approximately -120° to 120° in longitude on the ecliptic plane. Despite whether or not the modeled CME had a direct encounter with Earth, they created multiple disturbances in the vicinity of our planet. These can be identified in the animations for the solar-wind radial speed v_r and the magnetic-field components, radial (B_r), latitudinal B_{lat} , and longitudinal B_{lon} provided as supplementary materials. During the encounter with CMEs #7 and 8, Earth crossed the heliospheric current sheet (HCS). A detailed description on how this was identified both in time series and simulation output is provided in the [Appendix](#). This created a unique environment that is visualized in Figure 6.

A corotating interaction region (CIR) was reaching Earth and many of the simulated CMEs propagated through it. Of particular interest for our study is the interaction between CME #8 and this CIR. Another CIR had already passed Earth earlier in the simulation; some of the CMEs propagated through it, particularly after it had moved past Earth. A part of CME #7 (spheromak CME) interacted with it. The top-left panel in Figure 6 shows the solar-wind speed in the ecliptic plane, while the top-right panel – in the Earth's meridional plane. The bottom panel shows the spherical shell at a radial distance of 1 AU represented in 2D. As seen, at the time of the ACRE event onset at ca. 09 UT on 5 November 2023, there was no strong heliospheric disturbance hitting Earth, but there was a very strong sheath formed by CME #7 North-West of Earth at a distance of about 0.3–0.4 AU. Another sheath hit Earth several hours later, at ca. 17 UT of the same day causing a major geomagnetic storm. However, considering that the ACRE event was highly anisotropic with the CR flux arriving from nearly the anti-Sun direction, this approaching sheath could not be the source of the ACRE as otherwise, it would have produced anisotropy from the Sun's direction.

Thus, from the analysis of the heliospheric conditions, including direct modeling by EU-HFORIA, we conclude that at the time of the ACRE event, there was no major disturbance near Earth, which was crossing the HCS, but there was a strong sheath passing by North-West of Earth. While the situation is qualitatively clear in that the ACRE was likely caused by a local scattering of GeV-range GCR particles at said passing-by sheath, full quantitative modeling of such a faint event appears impossible with the current heliospheric models. The situation in the Earth's immediate vicinity was greatly disturbed (see Figure 7 in the [Appendix](#)). The peak strength of the hourly averaged IMF was attained at the end of the ACRE event at 13:00 UT with a value of 37.4 nT, simultaneously with the lowest level of -33.2 nT of the B_y component. Just after the ACRE event, also the B_z component reached its minimum of -22.5 nT. At 15:00 UT, the maximum solar-wind pressure at the threshold of 18.9 nPa was observed. Later, the solar-wind density maximum of 43.6 N cm $^{-3}$ was found. In the next hour, the solar-wind proton temperature was at the highest level of 2.9×10^5 K.

5. Discussion and Conclusions

Propagation of CRs in the vicinity of Earth is influenced by magnetic-field and solar-wind plasma structures in the heliosphere, which is specifically important for the low-energy part, below several GeV. Random walk of magnetic-field lines, which can occur during significant IMF disturbances, as well as the presence of large magnetized structures can affect the spatial transport and diffusion of charged particles and accordingly modify their fluxes near Earth, which may become significantly anisotropic.

Herein, we present the discovery and analysis of the third known and the so-far strongest ACRE event, detected by the mid- and high-latitude NMs around mid-day (12 UT) of 5 November 2023. The absence of a SEP increase in the spaceborne data excludes the solar origin of the event. The CR particles responsible for the ACRE arrived from a nearly anti-Sun direction within a confined cone of about 50° . The magnetospheric origin of the ACRE event is excluded because of the detection of the event at polar NMs, mismatching time profiles of the event and geomagnetic storm, and the strong event's anisotropy. Thus, the only plausible explanation involves focusing of GCRs in strongly disturbed heliospheric conditions. The heliospheric conditions during the event were highly disturbed at ≈ 0.3 AU North-West of the Earth's location, as a result of the previously launched strong CME. This distance takes several typical Larmor radii of a 10-GeV proton (≈ 0.05 AU) but is much larger than that for a 1-GeV proton (< 0.01 AU). Accordingly, while the propagation of

low-energy CRs from the sheath was effectively diffusive leading to a significant attenuation and isotropization of the ACRE signal, midenergy particles (especially helium and heavier species with double rigidity for the same energy per nucleon compared to protons) could arrive at Earth more directionally. The fact that the Earth was crossing the HCS might have facilitated particle access. This view can qualitatively explain the observed pattern of ACRE that while the high-latitude (low P_c) NMs reported weak (mostly $< 2\%$ h) and nearly isotropic enhancement, the enhancement at midlatitude NMs was stronger (up to 6.4% h) and confined around the anti-Sun direction – see Figure 3. However, although the qualitative picture is plausible and consistent with observations, quantitative modeling of such a complex phenomenon is presently unfeasible, even with the best possible heliospheric model such as EUHFORIA. A detailed heliospheric MHD model needs to be coupled with a full local CR transport model to advance in the quantitative modeling of such events. Development of such models requires significant community-wide efforts and lies beyond the scope of this empirical study.

Appendix

The in-situ solar-wind data from the L1 point for the day of 5 November 2023 are shown in Figure 7 according to the OMNIWeb database. This is an extended version of Figure 5 in terms of datasets presented, but presenting a smaller interval of time in order to facilitate inspection of the different signatures.

Prior to the flux-rope arrival, there are signatures in the OMNI data that indicate an HCS crossing. In Figure 8, which presents a zoom into Figure 5, we can identify a drop of the B-field magnitude at around 08:38 UT on 4 November (blue dotted line), although not very steep (see top panel). This is associated with a reversal in the B_x component, taking place at that time. The density is overall too low to show the expected drop during the HCS crossing; however, the plasma beta (bottom panel) shows a characteristic increase after the crossing. These signatures are indicators of crossing the neutral line. At the time of writing this paper, pitch-angle distribution (PAD) data were not available at L1. However, these data could be found for STEREO-A that orbits the Sun at the same radial distance as Earth and was only 5.7 deg ahead of Earth in longitude and < 1 degree north of Earth in latitude. STEREO-A-based PADs are shown in Figure 9, where an HCS crossing can be seen at around 12:00 UT the same day. This can be identified as the sudden change in the pitch angle from 0 to 180 degrees, a signature characteristic of HCS crossings. At 12:45 UT on the same day, there are signatures in the OMNI data indicative of a possible second HCS crossing (see magenta dotted line in Figure 8), however, this is past the time of the HCS crossing indicated by PADs at STEREO-A ahead of Earth. This could be an indication of a complicated and extended sector separation or disturbed IMF and solar-wind plasma conditions due to CME transients. To offer a meaningful explanation, we try to explain this using the output from the data-driven heliospheric simulation.

The simulation yielded that Earth crossed the HCS starting at 15:00 UT on 4 November 2023, at the same time as the flank of one of the simulated eruptions (ICME) was encountering Earth. This can be seen in Figure 5 as the bump in the number density of the EUHFORIA time series (panel 5 of the figure, blue curve). This ICME was propagating southward of Earth, pushing the current sheet northward towards Earth and possibly having a leg encounter with Earth (see CME 1 indicated with magenta color in Figure 10). Two other modeled eruptions arrived at Earth soon after that denoted in the same figure as 2 and 3. The one was modeled as a hydrodynamic pulse and was propagating to the left of the HCS

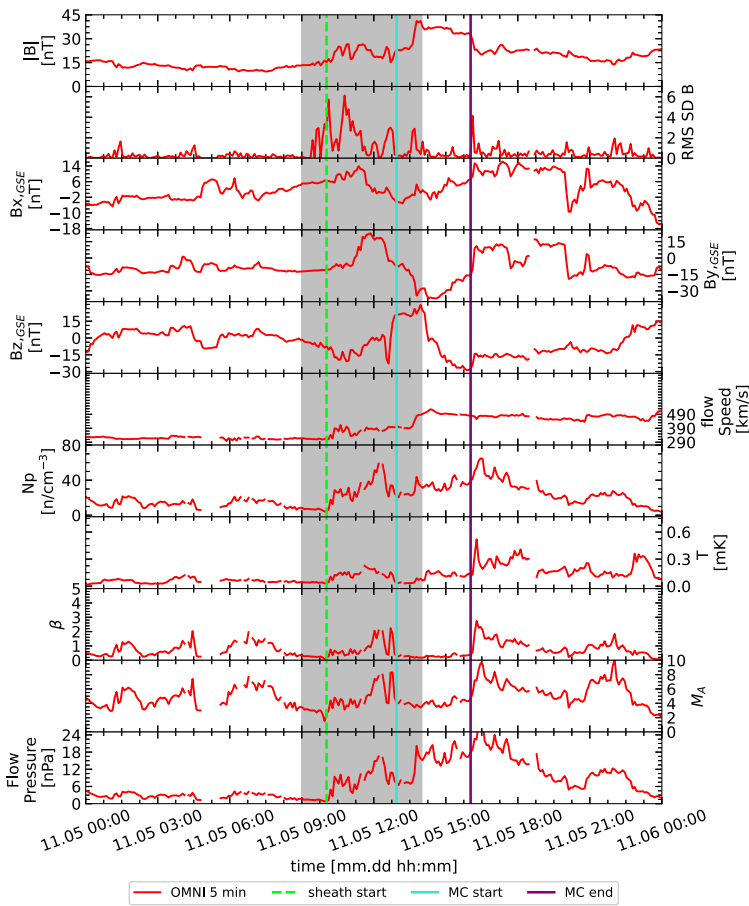


Figure 7 Extended version of Figure 5, centered around the flux rope arrival at Earth, including OMNI data (red curves) parameters of (top–down panels) magnetic-field magnitude $|B|$; and its three components B_x ; B_y ; B_z in GSE coordinates; plasma-flow speed; proton number density N_p ; temperature T_p ; plasma beta β ; Mach number M_A ; and plasma-flow pressure. The data were measured at the L1 point and translated to the near-Earth conditions by applying a 62-min delay corresponding to the propagation time from the L1 point for $V = 400 \text{ km s}^{-1}$. The shaded region denotes the time of the ACRE event. The green dashed line indicates the start of the sheath-region, while the cyan and purple solid lines indicate the identified start and end of MC, respectively.

(CME 2 in the figure). The other CME, modeled as a magnetized flux rope, was propagating to the right of the HCS (CME 3 in the figure). These two CMEs are well visible in Figure 6. Their evolution can be better seen in the animations provided as supplementary materials. Although the simulation time might not match exactly the measured time profiles thus making a quantitative conclusion difficult, we have reasons to believe that a possible interaction between the three CMEs and the HCS could be responsible for the complicated OMNI signatures marked as possibly associated with HCs crossing signatures in Figure 8 (magenta dotted line) and the complicated sheath that started at around 09:00 UT on 5 November at OMNI data.

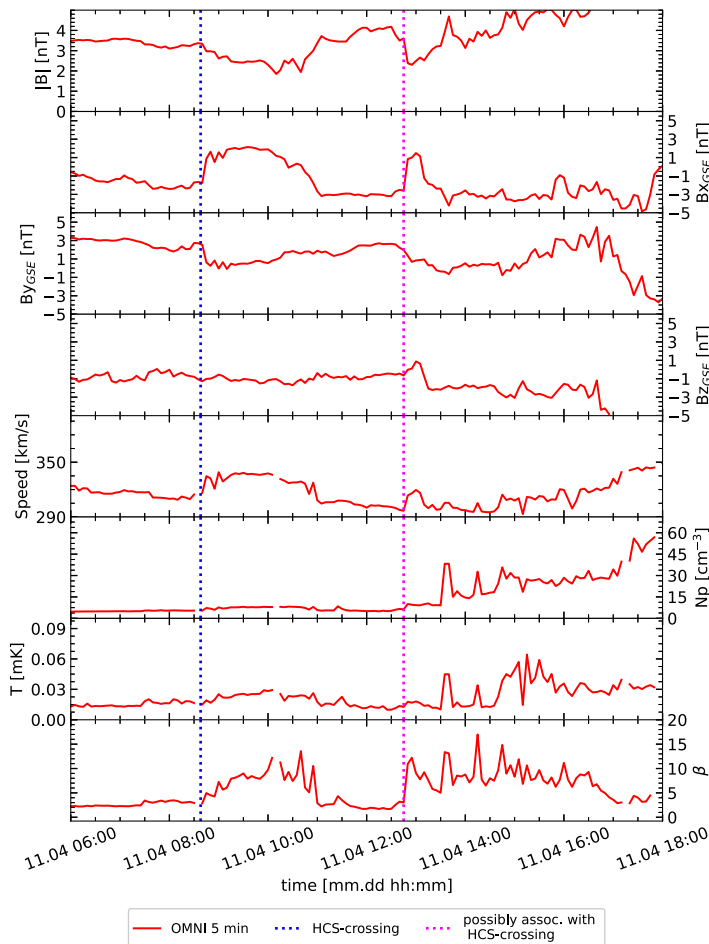


Figure 8 OMNI data for a smaller time window of that presented in Figure 5 focusing on the HCS crossing indicated by the blue dotted line. The magenta dotted line denotes signatures in the data that are indicative of a HCS crossing as well, but that, however, is followed by more complex signatures.

This could potentially affect the GCR intensity since positively charged GCR particles drift outward along the HCS during a positive-polarity epoch of the IMF (which is the case during this event). Thus, we anticipate an impact of interplanetary CMEs–HCS interplay on the GCR fluxes arriving at Earth. This is only a qualitative and to some extent speculative conclusion, but it is presently impossible to model particle transport during these conditions and validate it.

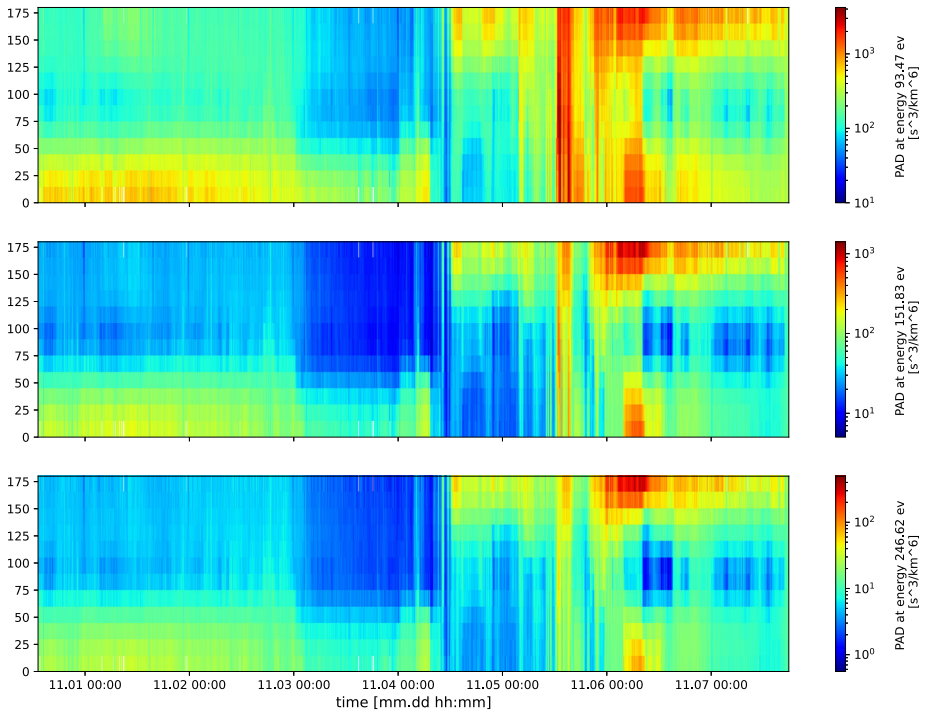


Figure 9 Pitch-angle distributions at STEREO-A from three energy channels 93.47 eV (top panel), 151.83 eV (middle panel), 246.62 eV (bottom panel).

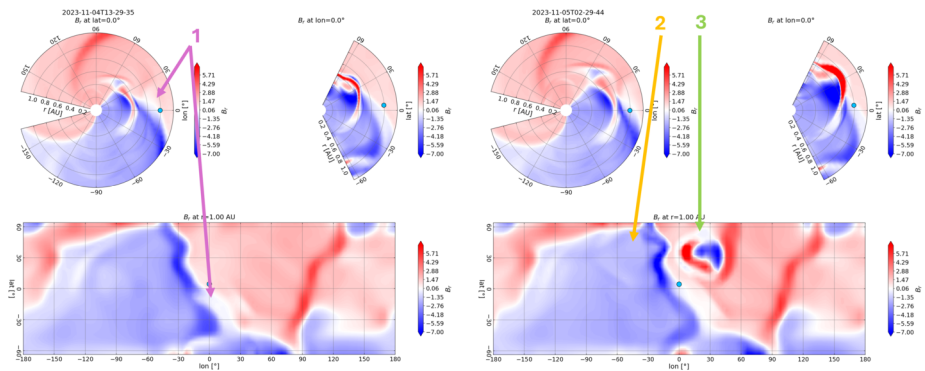


Figure 10 Three slice images of the simulation output, similar to that given in Figure 6, but presenting the B_r magnetic component. The arrows indicate 3 of the modeled ICME signatures that are relevant for understanding the near-Earth conditions. ICMEs 2 is faint here but it is clearly visible also in Figure 6.

Supplementary Information The online version contains supplementary material available at <https://doi.org/10.1007/s11207-024-02338-3>.

Acknowledgments We acknowledge all the PIs and colleagues from the NMs, who kindly provided the data used in this analysis. Du Toit Strauss is acknowledged for sharing the 1-min data from South African NMs. Eleanna Asvestari is thankful to Dr. Tobias Rindlisbacher for the fruitful discussions on the spheromak insertion orientation. Italian polar program PNRA (via the AIR-FLOC PNRA OSS-04 project), the French Polar Institute IPEV and the Finnish Antarctic Research Program (FINNARP) are acknowledged for the hosting of DOMC/B NM. We acknowledge the Community Coordinated Modeling Center (CCMC) at Goddard Space Flight Center for the use of the StereoCAT tool, ccmc.gsfc.nasa.gov/tools/StereoCat/. The OMNI data were obtained from the GSFC/SPDF OMNIWeb interface at omniweb.gsfc.nasa.gov. Data for the OTSO AC computations was obtained from the NASA and ESA co-owned SOHO database sohoftp.nascom.nasa.gov/ and, the Kyoto University-hosted World Data Center for Geomagnetism (wdc.kugi.kyoto-u.ac.jp/), to whom we extend our thanks for the use of their publicly accessible databases. We acknowledge the support of the International Space Science Institute (Bern, Switzerland), Visiting Fellowship Program, and International Teams No. 475 (Modeling Space Weather And Total Solar Irradiance Over The Past Century) and No. 585 (RE-ASSESS).

Author contributions A.G. was responsible for the collection and analysis of the neutron monitor data, E.A. performed modelling of the heliospheric conditions with the EUHFORIA model, A.M. and N.L. performed computations and analysis of the magnetospheric transport of energetic particles, I.U. led the interpretation of the results and supervised the analysis. All the co-authors equally contributed to the writing of the paper.

Funding Open Access funding provided by University of Oulu (including Oulu University Hospital). Eleanna Asvestari acknowledges support from the Academy of Finland/Research Council of Finland (Academy Research Fellow grant number 355659). This study was partly supported by the Research Council of Finland (project 330063 QUASARE and 354280 GERACLIS). The work was partially supported by the Horizon Europe program projects ALBATROS and SPEARHEAD. This work was also partially supported by the National Science Fund of Bulgaria under contract KP-06-H28/4.

Data Availability No datasets were generated or analysed during the current study.

Declarations

Competing interests The authors declare no competing interests.

Open Access This article is licensed under a Creative Commons Attribution 4.0 International License, which permits use, sharing, adaptation, distribution and reproduction in any medium or format, as long as you give appropriate credit to the original author(s) and the source, provide a link to the Creative Commons licence, and indicate if changes were made. The images or other third party material in this article are included in the article's Creative Commons licence, unless indicated otherwise in a credit line to the material. If material is not included in the article's Creative Commons licence and your intended use is not permitted by statutory regulation or exceeds the permitted use, you will need to obtain permission directly from the copyright holder. To view a copy of this licence, visit <http://creativecommons.org/licenses/by/4.0/>.

References

- Abunin, A.A., Abunina, M.A., Belov, A.V., Chertok, I.M.: 2020, Peculiar solar sources and geospace disturbances on 20–26 August 2018. *Solar Phys.* **295**, 7. DOI. ADS.
- Alken, P., Thébault, E., Beggan, C.D., Amit, H., Aubert, J., Baerenzung, J., Bondar, T.N., Brown, W.J., Califf, S., Chambodut, A., Chulliat, A., Cox, G.A., Finlay, C.C., Fournier, A., Gillet, N., Grayver, A., Hammer, M.D., Holschneider, M., Huder, L., Hulot, G., Jager, T., Kloss, C., Korte, M., Kuang, W., Kuvshinov, A., Langlais, B., Léger, J.-M., Lesur, V., Livermore, P.W., Lowes, F.J., Macmillan, S., Magnes, W., Manda, M., Marsal, S., Matzka, J., Metman, M.C., Minami, T., Morschhauser, A., Mound, J.E., Nair, M., Nakano, S., Olsen, N., Pavón-Carrasco, F.J., Petrov, V.G., Ropp, G., Rother, M., Sabaka, T.J., Sanchez, S., Saturnino, D., Schnepf, N.R., Shen, X., Stolle, C., Tangborn, A., Tøffner-Clausen, L., Toh, H., Torta, J.M., Varner, J., Vervelidou, F., Vigneron, P., Wardinski, I., Wicht, J., Woods, A., Yang, Y., Zeren, Z., Zhou, B.: 2021, International geomagnetic reference field: the thirteenth generation. *Earth Planets Space* **73**, 49. DOI. ADS.

- Arge, C.N., Henney, C.J., Koller, J., Compeau, C.R., Young, S., MacKenzie, D., Fay, A., Harvey, J.W.: 2010, Air Force Data Assimilative Photospheric Flux Transport (ADAPT) model. In: Maksimovic, M., Is-sautier, K., Meyer-Vernet, N., Moncuquet, M., Pantellini, F. (eds.) *Twelfth International Solar Wind Conference, American Institute of Physics Conference Series* **1216**, 343. DOI. ADS.
- Asvestari, E., Pomoell, J., Kilpua, E., Good, S., Chatzistergos, T., Temmer, M., Palmerio, E., Poedts, S., Magdalenic, J.: 2021, Modelling a multi-spacecraft coronal mass ejection encounter with EUHFORIA. *Astron. Astrophys.* **652**, A27. DOI. ADS.
- Asvestari, E., Rindlisbacher, T., Pomoell, J., Kilpua, E.K.J.: 2022, The spheromak tilting and how it affects modeling coronal mass ejections. *Astrophys. J.* **926**, 87. DOI. ADS.
- Belov, A.V., Abunina, M.A., Abunin, A.A., Eroshenko, E.A., Oleneva, V.A., Yanke, V.G.: 2017, Vector anisotropy of cosmic rays in the beginning of Forbush effects. *Geomagn. Aeron.* **57**, 541. DOI. ADS.
- Bieber, J.W., Evenson, P., Dröge, W., Pyle, R., Ruffolo, D., Rujiwarodom, M., Tooprakai, P., Khumlumlert, T.: 2004, Spaceship Earth observations of the easter 2001 solar particle event. *Astrophys. J. Lett.* **601**, L103. DOI. ADS.
- Breckner, G.E., Howard, R.A., Koomen, M.J., Korendyke, C.M., Michels, D.J., Moses, J.D., Socker, D.G., Dere, K.P., Lamy, P.L., Llebaria, A., Bout, M.V., Schwenn, R., Simnett, G.M., Bedford, D.K., Eyles, C.J.: 1995, The Large Angle Spectroscopic Coronagraph (LASCO). *Solar Phys.* **162**, 357. DOI. ADS.
- Bütikofer, R.: 2018, Cosmic ray particle transport in the Earth's magnetosphere. In: *Solar Particle Radiation Storms Forecasting and Analysis, the HESPERIA HORIZON 2020 Project and Beyond* **79**, Springer, Cham. Chapter 5. ISBN 978-3-319-60051-2.
- Cane, H.V.: 2000, Coronal mass ejections and Forbush decreases. *Space Sci. Rev.* **93**, 55. DOI. ADS.
- Carmichael, H., Bercovitch, M., Shea, M.A., Magidin, M., Peterson, R.W.: 1968, Attenuation of neutron monitor radiation in the atmosphere. *Can. J. Phys.* **46**, 1006.
- Clem, J.M., Dorman, L.L.: 2000, Neutron monitor response functions. *Space Sci. Rev.* **93**, 335. DOI. ADS.
- Cooke, D.J., Humble, J.E., Shea, M.A., Smart, D.F., Lund, N., Rasmussen, I.L., Byrnak, B., Goret, P., Petrou, N.: 1991, On cosmic-ray cut-off terminology. *Nuovo Cimento C* **14**, 213. ADS.
- Desai, M., Giacalone, J.: 2016, Large gradual solar energetic particle events. *Living Rev. Solar Phys.* **13**, 3. DOI. ADS.
- Domingo, V., Fleck, B., Poland, A.I.: 1995, The SOHO mission: an overview. *Solar Phys.* **162**, 1. DOI. ADS.
- Dumbović, M., Vršnak, B., Temmer, M., Heber, B., Köhl, P.: 2022, Generic profile of a long-lived corotating interaction region and associated recurrent Forbush decrease. *Astron. Astrophys.* **658**, A187. DOI. ADS.
- Gil, A., Kovaltsov, G.A., Mikhailov, V.V., Mishev, A., Poluianov, S., Usoskin, I.G.: 2018, An anisotropic cosmic-ray enhancement event on 07-June-2015: a possible origin. *Solar Phys.* **293**, 154. DOI. ADS.
- Hatton, C.J., Carimichael, H.: 1964, Experimental investigation of the NM-64 neutron monitor. *Can. J. Phys.* **42**, 2443. DOI. ADS.
- Iyemori, T., Takeda, M., Nose, M., Odagi, Y., Toh, H.: 1996, Mid-latitude Geomagnetic Indices "ASY" and "SYM" for 2009 (Provisional). <https://wdc.kugi.kyoto-u.ac.jp/aeasy/asy.pdf>.
- Jämsén, T., Usoskin, I.G., Rähkä, T., Sarkamo, J., Kovaltsov, G.A.: 2007, Case study of Forbush decreases: energy dependence of the recovery. *Adv. Space Res.* **40**, 342. DOI. ADS.
- Kaiser, M.L.: 2005, The STEREO mission: an overview. *Adv. Space Res.* **36**, 1483. DOI. ADS.
- Kaiser, M.L., Kucera, T.A., Davila, J.M., St. Cyr, O.C., Guhathakurta, M., Christian, E.: 2008, The STEREO mission: an introduction. *Space Sci. Rev.* **136**, 5. DOI. ADS.
- King, J.H., Papitashvili, N.E.: 2005, Solar wind spatial scales in and comparisons of hourly wind and ACE plasma and magnetic field data. *J. Geophys. Res. Space Phys.* **110**, A02104. DOI. ADS.
- Kudela, K., Bučfk, R., Bobfk, P.: 2008, On transmissivity of low energy cosmic rays in disturbed magnetosphere. *Adv. Space Res.* **42**, 1300. DOI. ADS.
- Larsen, N., Mishev, A., Usoskin, I.: 2023, A new open-source geomagnetosphere propagation tool (OTSO) and its applications. *J. Geophys. Res. Space Phys.* **128**, e2022JA031061. DOI. ADS.
- Mavromichalaki, H., Papaioannou, A., Plainaki, C., Sarlanis, C., Souvatzoglou, G., Gerontidou, M., Papailiou, M., Eroshenko, E., Belov, A., Yanke, V., Flückiger, E.O., Bütikofer, R., Parisi, M., Storini, M., Klein, K.-L., Fuller, N., Steigies, C.T., Rother, O.M., Heber, B., Wimmer-Schweingruber, R.F., Kudela, K., Strharsky, I., Langer, R., Usoskin, I., Ibragimov, A., Chilingaryan, A., Hovsepian, G., Reymers, A., Yeghikyan, A., Kryakunova, O., Dryn, E., Nikolayevskiy, N., Dorman, L., Pustil'Nik, L.: 2011, Applications and usage of the real-time neutron monitor database. *Adv. Space Res.* **47**, 2210. DOI. ADS.
- Mishev, A., Poluianov, S.: 2021, About the altitude profile of the atmospheric cut-off of cosmic rays: new revised assessment. *Solar Phys.* **296**, 129. DOI.
- Mishev, A.L., Poluianov, S., Usoskin, I.: 2017, Assessment of spectral and angular characteristics of sub-GLE events using the global neutron monitor network. *J. Space Weather Space Clim.* **7**, A28. DOI. ADS.
- Mishev, A., Usoskin, I.: 2020, Current status and possible extension of the global neutron monitor network. *J. Space Weather Space Clim.* DOI.

- Palmerio, E., Kilpua, E.K.J., James, A.W., Green, L.M., Pomoell, J., Isavnin, A., Valori, G.: 2017, Determining the intrinsic CME flux rope type using remote-sensing solar disk observations. *Solar Phys.* **292**, 39. DOI. ADS.
- Papailiou, M., Abunina, M., Mavromichalaki, H., Belov, A., Abunin, A., Eroshenko, E., Yanke, V.: 2021, Precursory signs of large Forbush decreases. *Solar Phys.* **296**, 100. DOI. ADS.
- Pevtsov, A.A., Balasubramaniam, K.S.: 2003, Helicity patterns on the sun. *Adv. Space Res.* **32**, 1867. DOI. ADS.
- Poedts, S., Lani, A., Scolini, C., Verbeke, C., Wijsen, N., Lapenta, G., Laperre, B., Millas, D., Innocenti, M.E., Chané, E., Baratashvili, T., Samara, E., Van der Linden, R., Rodriguez, L., Vanlommel, P., Vainio, R., Afanasiev, A., Kilpua, E., Pomoell, J., Sarkar, R., Aran, A., Sanahuja, B., Paredes, J.M., Clarke, E., Thomson, A., Rouillard, A., Pinto, R.F., Marchaudon, A., Blelly, P.-L., Gorce, B., Plotnikov, I., Kouloumvakos, A., Heber, B., Herbst, K., Kochanov, A., Raeder, J., Depauw, J.: 2020, European heliospheric FORecasting information asset 2.0. *J. Space Weather Space Clim.* **10**, 57. DOI. ADS.
- Poluianov, S.V., Usoskin, I.G., Mishev, A.L., Shea, M.A., Smart, D.F.: 2017, GLE and sub-GLE redefinition in the light of high-altitude polar neutron monitors. *Solar Phys.* **292**, 176. DOI. ADS.
- Pomoell, J., Poedts, S.: 2018, EUHFORIA: European heliospheric forecasting information asset. *J. Space Weather Space Clim.* **8**, A35. DOI. ADS.
- Potgieter, M.: 2013, Solar modulation of cosmic rays. *Living Rev. Solar Phys.* **10**, 3. DOI. ADS.
- Reames, D.V.: 2017, *Solar Energetic Particles, Lecture Notes in Physics* **932**, Springer, Berlin. DOI. ADS.
- Riley, P., Mays, M.L., Andries, J., Amerstorfer, T., Biesecker, D., Delouille, V., Dumbović, M., Feng, X., Henley, E., Linker, J.A., Möstl, C., Nuñez, M., Pizzo, V., Temmer, M., Tobiska, W.K., Verbeke, C., West, M.J., Zhao, X.: 2018, Forecasting the arrival time of coronal mass ejections: analysis of the CCMC CME scoreboard. *Space Weather* **16**, 1245. DOI. ADS.
- Sarkar, R., Pomoell, J., Kilpua, E., Asvestari, E., Wijsen, N., Maharana, A., Poedts, S.: 2024, Studying the spheromak rotation in data-constrained coronal mass ejection modeling with EUHFORIA and assessing its effect on the B_z prediction. *Astrophys. J. Suppl.* **270**, 18. DOI. ADS.
- Simpson, J.: 1957, Cosmic-radiation neutron intensity monitor. *Ann. Int. Geophys. Year* **4**, 351.
- Simpson, J.A.: 2000, The cosmic ray nucleonic component: the invention and scientific uses of the neutron monitor. *Space Sci. Rev.* **93**, 11. DOI. ADS.
- Simpson, J.A., Fonger, W., Treiman, S.B.: 1953, Cosmic radiation intensity-time variations and their origin. I. Neutron intensity variation method and meteorological factors. *Phys. Rev.* **90**, 934. DOI. ADS.
- Smart, D.F., Shea, M.A., Flückiger, E.O.: 2000, Magnetospheric models and trajectory computations. *Space Sci. Rev.* **93**, 305. DOI. ADS.
- Sugiura, M., Poros, D.J.: 1971, Hourly values of equatorial Dst for years 1957 to 1970. <https://ntrs.nasa.gov/api/citations/19710022962/downloads/19710022962.pdf>.
- Tsyganenko, N.A.: 2002, A model of the near magnetosphere with a dawn-dusk asymmetry. *J. Geophys. Res. Space Phys.* **107**, 1179. DOI.
- Usoskin, I.G., Braun, I., Gladysheva, O.G., Hörandel, J.R., Jämsén, T., Kovaltsov, G.A., Starodubtsev, S.A.: 2008, Forbush decreases of cosmic rays: energy dependence of the recovery phase. *J. Geophys. Res.* **113**, A07102. DOI. ADS.
- Usoskin, I.G., Koldobskiy, S., Kovaltsov, G.A., Gil, A., Usoskina, I., Willamo, T., Ibragimov, A.: 2020a, Revised GLE database: fluences of solar energetic particles as measured by the neutron-monitor network since 1956. *Astron. Astrophys.* **640**, A17. DOI. ADS.
- Usoskin, I.G., Koldobskiy, S.A., Kovaltsov, G.A., Rozanov, E.V., Sukhodolov, T.V., Mishev, A.L., Mironova, I.A.: 2020b, Revisited reference solar proton event of 23 February 1956: assessment of the cosmogenic-isotope method sensitivity to extreme solar events. *J. Geophys. Res. Space Phys.* **125**, e27921. DOI. ADS.
- Vainio, R., Desorgher, L., Heynderickx, D., Storini, M., Flückiger, E., Horne, R.B., Kovaltsov, G.A., Kudela, K., Laurenza, M., McKenna-Lawlor, S., Rothkaehl, H., Usoskin, I.G.: 2009, Dynamics of the Earth's particle radiation environment. *Space Sci. Rev.* **147**, 187. DOI.
- Verbeke, C., Pomoell, J., Poedts, S.: 2019, The evolution of coronal mass ejections in the inner heliosphere: implementing the spheromak model with EUHFORIA. *Astron. Astrophys.* **627**, A111. DOI. ADS.
- Verbeke, C., Mays, M.L., Temmer, M., Bingham, S., Steenburgh, R., Dumbović, M., Nuñez, M., Jian, L.K., Hess, P., Wiegand, C., Taktakishvili, A., Andries, J.: 2019, Benchmarking CME arrival time and impact: progress on metadata, metrics, and events. *Space Weather* **17**, 6. DOI. ADS.
- Wang, Y.-M.: 2013, On the strength of the hemispheric rule and the origin of active-region helicity. *Astrophys. J. Lett.* **775**, L46. DOI. ADS.